Journal of ELECTRONIC MATERIALS, Vol. 41, No. 10, 2012
DOI: 10.1007/s11664-012-2182-7

Electrooptical Characterization of MWIR InAsSb Detectors

A.I. D'SOUZA,[1,6] E. ROBINSON,[1] A.C. IONESCU,[1] D. OKERLUND,[1]
T.J. DE LYON,[2] H. SHARIFI,[2] M. ROEBUCK,[2] D. YAP,[2] R.D. RAJAVEL,[2]
N. DHAR,[3] P.S. WIJEWARNASURIYA,[4] and C. GREIN[5]

1.—DRS Sensors and Targeting Systems, 10600 Valley View Street, Cypress, CA 90630, USA. 2.—HRL Laboratories, LLC, 3011 Malibu Canyon Rd., Malibu, CA 90265, USA. 3.—DARPA, MTO, 3701 N. Fairfax Dr., Arlington, VA 22203, USA. 4.—U.S. Army Research Laboratory, 2800 Powder Mill Road, Adelphi, MD 20783, USA. 5.—University of Illinois at Chicago, 845 W. Taylor St., Chicago, IL 60607, USA. 6.—e-mail: arvind.d'souza@drs-sts.com

$InAs_{1-x}Sb_x$ material with an alloy composition of the absorber layer adjusted to achieve 200-K cutoff wavelengths in the 5-μm range has been grown. Compound-barrier (CB) detectors were fabricated and tested for optical response, and J_{dark}–V_{d} measurements were taken as a function of temperature. Based on absorption coefficient information in the literature and spectral response measurements of the midwave infrared (MWIR) nCBn detectors, an absorption coefficient formula $\alpha(\mathrm{E}, x, T)$ is proposed. Since the presently suggested absorption coefficient is based on limited data, additional measurements of material and detectors with different x values and as a function of temperature should refine the absorption coefficient, providing more accurate parametrization. Material electronic structures were computed using a $k{\cdot}p$ formalism. From the band structure, dark-current density (J_{dark}) as a function of bias (V_{d}) and temperature (T) was calculated and matched to J_{dark}–V_{d} curves at fixed T and J_{dark}–T curves at constant V_{d}. There is a good match between simulation and data over a wide range of bias, but discrepancies that are not presently understood exist near zero bias.

Key words: MWIR barrier detectors, photon-trap structures

INTRODUCTION

The AWARE Broadband program requires an innovative detector architecture and processing techniques to achieve pioneering performance of MWIR detectors at 200 K. One of the ambitious requirements is to obtain high (>80%) quantum efficiency (QE) over a broad, 0.5 μm to 5.0 μm spectral range while maintaining high D^* ($>1.0 \times 10^{11}$ cm $\sqrt{\mathrm{Hz}}$/W) in the 3.0 μm to 5.0 μm spectral range. A prime method to accomplish these goals is by reducing the dark diffusion current in the detector via reducing the volume fill ratio (VFR) of the detector while optimizing absorption through the design of photon-trap topological structures in the absorber layer upon which the radiation is incident. For the program, InAsSb was chosen as the absorber layer of the multilayer compound-barrier detector architecture.

MWIR photodetector performance improvements were realized through the development of devices that rely upon bandgap engineering for the reduction of dark currents associated with depletion-region Shockley–Read–Hall (SRH) generation, surface current generation, and bulk diffusion. In particular, the nBn[1,2] device in the InAsSb/AlAsSb materials system is based on a simple design that utilizes a large conduction-band barrier to suppress the flow of majority carrier electrons, thus eliminating the electric field associated with a conventional p–n junction that results in high dark currents associated with depletion-region generation–recombination currents. Thus, a properly designed nBn structure facilitates diffusion-dominated detector performance determined by the bulk minority carrier (hole) lifetime.

(Received October 21, 2011; accepted June 16, 2012;

DETECTOR ARCHITECTURE

Innovative nBn barrier detectors[1,2] were designed to suppress majority carrier currents while maintaining low electric fields. This nBn design was considered a remedy to the generation–recombination currents originating in the depletion region of *p–n* junction devices. AlAsSb alloy is used as a wide-bandgap barrier material, due to its having no significant valence-band offset with respect to InAsSb, which facilitates collection of minority carriers (holes) while providing a large barrier to majority carriers. However, the original InAsSb/AlAsSb barrier device design can have potential deficiencies associated with the choice of AlAsSb as the barrier material due to the alignment between the active layer and the barrier. Circumventing some of the difficulties inherent to the original nBn design, a compound-barrier (CB) detector architecture[3] was designed and implemented with the alloy composition of the InAsSb absorber layer adjusted to achieve a 200-K cutoff wavelength of 4.3 μm.[4,5] The novel detector structure, which is displayed in Fig. 1, utilizes pyramid-shaped absorbers. Each detector pixel has an array of multiple pyramid-shaped absorbers. This detector structure provides the combination of reduced volume of absorber material, elimination of front-side reflection for incident light over a broad bandwidth, and enhanced photon trapping for high absorbance of incident light.

Infrared radiation is incident on the array of pyramids fabricated in the *n*-type InAsSb absorber, which also serves as the array common or substrate contact. The detector array is hybridized via indium bumps to a Si fanout chip. The chip, when inserted into an 84-pin leadless chip carrier (LCC), permits direct access to approximately 80 detectors. Detector areas ranged from 3.6×10^{-5} cm^2 to 1.15×10^{-3} cm^2. The common contact to the absorber layer is a remote contact, and adjacent detectors were not biased during measurement of the reference detector.

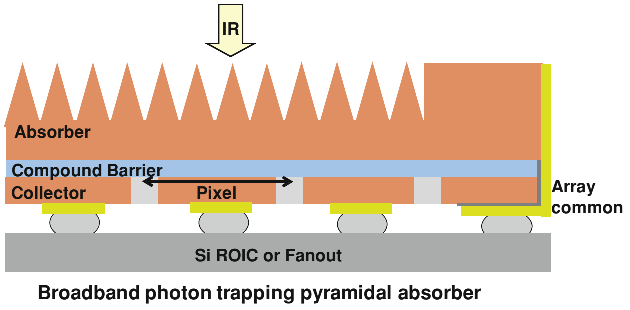

Fig. 1. Compound-barrier detector architecture with pyramid-shaped absorber layer.

MATERIAL AND DETECTOR MODELING

Modeling InAs$_{1-x}$Sb$_x$-based device performance requires obtaining experimental and/or theoretical material parameters. InAs$_{1-x}$Sb$_x$ is a ternary compound whose bandgap changes as a function of x and temperature T. Clear-cut experimental or theoretical information on InAs$_{1-x}$Sb$_x$(x, T) is sparse, therefore requiring the utilization of approximations that "best" fit the data or equations available, and then generalizing the model.

Bandgap $E_g(x, T)$ and Cutoff Wavelength λ_c

The InAs$_{1-x}$Sb$_x$ bandgap[4,5] $E_g(x, T)$ in eV is given by Eq. 1, and to a first approximation the cutoff wavelength is given by Eq. 2. The cutoff wavelength as a function of x at temperature T = 200 K is displayed in Fig. 2. The bandgap and cutoff wavelength at any other temperature can be calculated using Eqs. 1 and 2.

$$E_g(x,T) = 0.411 - \frac{3.4 \times 10^{-4} T^2}{210 + T} - 0.867x + 0.70x^2 + 3.4 \times 10^{-4} xT(1-x). \tag{1}$$

To a first approximation, the cutoff wavelength λ_c in microns is

$$\lambda_c(x,T) = \frac{1.2398}{E_g(x,T)}. \tag{2}$$

Using these expressions, $x \approx 0.21$ gives λ_c = 5.25 μm at T = 200 K.

Absorption Coefficient $\alpha(\lambda, x, T)$

Absorption coefficient information for InAs above the bandgap[6] at room temperature and separately

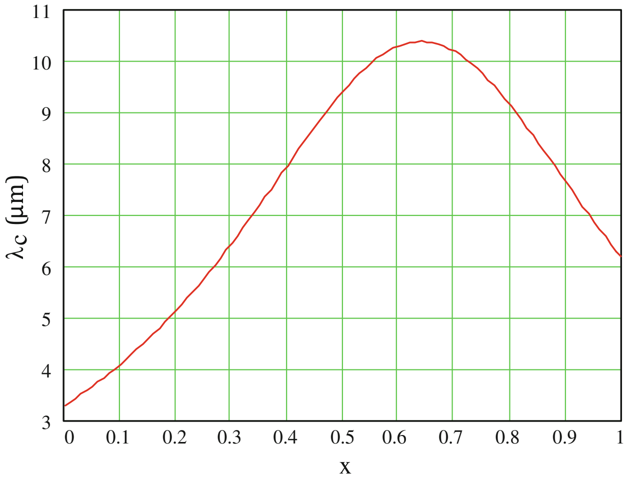

Fig. 2. Variation in InAs$_{1-x}$Sb$_x$ cutoff wavelength λ_c as a function of x at T = 200 K.

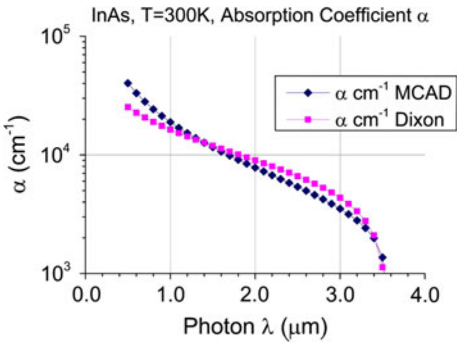

Fig. 3. Match between $\alpha(\lambda,\ x = 0,\ T = 300$ K) from the literature ("Dixon")[5] and calculated using Eqs. 3a, b and 4a–c ("MCAD"). MCAD is a software package (Mathcad) marketed by Mathcad uses to perform engineering calculations.

data for various x values for below-bandgap photon energies[7] is available in the literature. An empirical expression is suggested to best match the limited available data. Above the bandgap, the expression of Moazzami et al.[8] was modified so that $\alpha(E_g)$ does not drop to zero but gives a value at the energy gap $\alpha(E_g) = 800\ \text{cm}^{-1}$. Energies below the bandgap utilize the Urbach tail[9] expression. The constants in Eqs. 3a, b were picked to best replicate below-bandgap data in Ref. 6. Above the bandgap, the coefficients K and c in Eqs. 4a–c were picked to give values that attempted to match calculations made using the expression for InAs at $T = 300$ K found in Ref. 6. Shown in Fig. 3 is the absorption coefficient $\alpha(\lambda,\ x = 0,\ T = 300\ \text{K})$, i.e., for InAs at $T = 300$ K. Use of Eqs. 3 and 4 permits one to calculate the absorption coefficient as a function of wavelength, x, and T, as shown in Fig. 4 for $x = 0.19$ and $T = 200$ K, i.e., for $\lambda \approx 5.05\ \mu$m at 200 K. The constants used in Eqs. 3 and 4 are not unique and will require refining as more absorption coefficient and spectral response data are acquired or become available. This section attempted to collate material properties from several sources, and an equation for the absorption coefficient was developed to best match the available data. The absorption coefficient in Eqs. 3 and 4 will be utilized to calculate the absorption coefficient versus wavelength for a MWIR $InAs_{0.81}Sb_{0.19}$-based detector at 200 K. Further investigation into the spectral response of $InAs_{1-x}Sb_x$ detectors will test the utility of the following absorption coefficient expressions.

For photon energies $E \leq E_g$,

$$\alpha(E,x,T) = 948.23 \times e^{170(E-E_0)} \quad E_0 = E_g + 0.001. \tag{3a, b}$$

For photon energies $E > E_g$,

$$\alpha(E,x,T) = \frac{\left[K(E-E_g-c)\sqrt{(E-E_g-c)^2 - c^2}\right]}{E} + 800 \quad c = 0.5E_g + 0.1$$
$$K = 10000 + 20000E_g. \tag{4a-b}$$

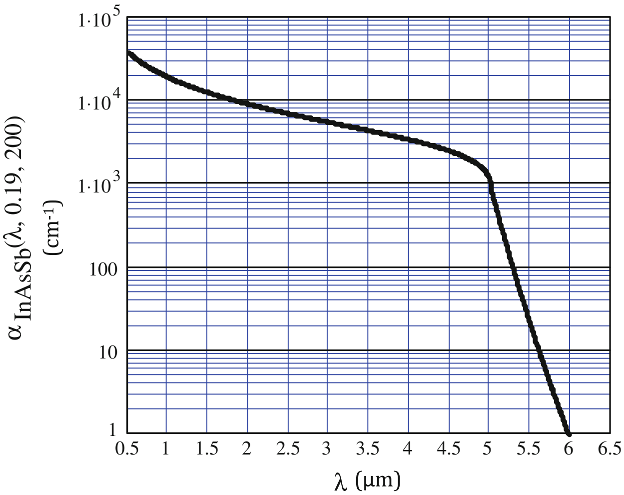

Fig. 4. $InAs_{0.81}Sb_{0.19}$ absorption coefficient versus wavelength at $T = 200$ K using Eqs. 3 and 4.

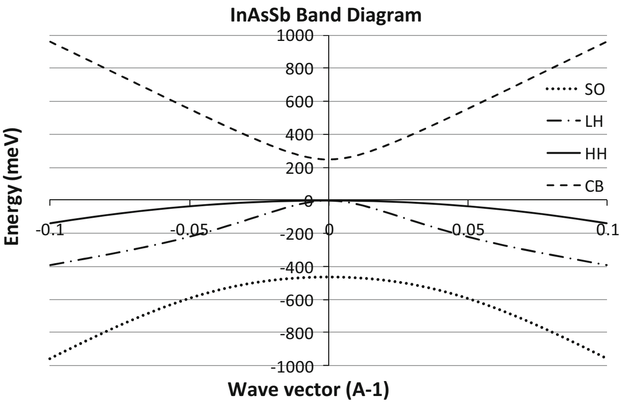

Fig. 5. Computed band structure diagram for $InAs_{1-x}Sb_x$ with $x = 0.19$ at $T = 200$ K.

Band Structure

The material electronic structures were computed with a $k{\cdot}p$ formalism.[10] The zone-center states are calculated in Fourier space using a 14-band basis. The need to rely on a 14-band basis rather than the more common 8-band basis arises because of the sensitivity of the optical and electronic properties to the electronic structure in the secondary regions of the band structure. Errors inherent in the 8-band model become significantly more pronounced as the states one is interested in become farther from the band edge.[10,11] Results of the $InAs_{1-x}Sb_x$ electronic structure calculations for $x = 0.19$ at $T = 200$ K are displayed as a band structure plot in Fig. 5.

Figures 6a, b and 7a, b show the conduction and valence bands through the nCBn detector at bias values $V_d = -0.2$ V, -0.4 V, -1.4 V, and -3.0 V, respectively. The n-type $InAs_{1-x}Sb_x$ absorber region, which may be a ~5-μm-thick layer or a thin layer contoured with pyramids, is at the left of

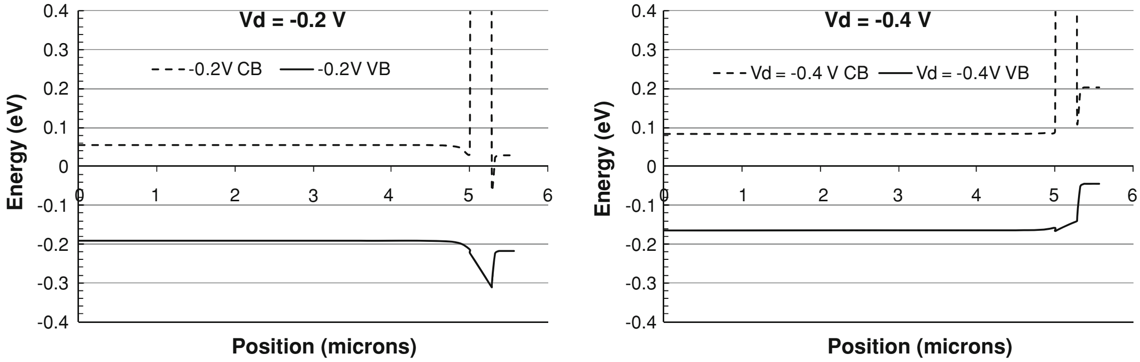

Fig. 6. Computed conduction (CB) and valence bands (VB) at (a) $V_d = -0.2$ V and (b) $V_d = -0.4$ V through the nCBn detector.

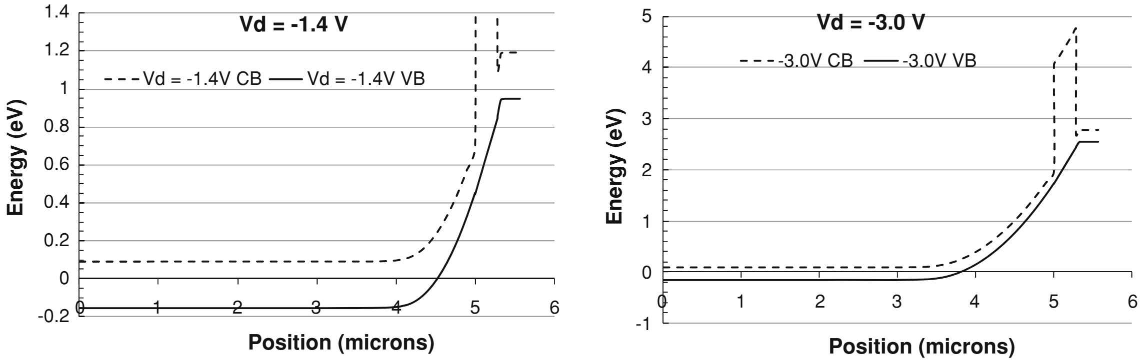

Fig. 7. Computed conduction (CB) and valence bands (VB) at (a) $V_d = -1.4$ V and (b) $V_d = -3.0$ V through the nCBn detector.

Figs. 6a, g and 7a, b. In all references through this paper, the bias sign convention is for bias applied to the n^+ contact region. In other words, a bias listed as $V_d = -0.4$ V implies a bias of -0.4 V applied to the n^+ contact layer while the n-type absorber layer is held at zero bias, or conversely that the n^+ contact layer is held at zero bias while a +0.4 V bias is applied to the n-type absorber layer. As can be seen from Fig. 6a, there is still a $\sim$100 meV valence-band barrier when $V_d = -0.2$ V is applied to the n^+ contact layer. Therefore, it should be expected that the QE will be low at $V_d = -0.2$ V. At $V_d = -0.4$ V, the valence-band barrier is virtually nonexistent and the QE should be high. At $V_d = -1.4$ V and -3.0 V, there is no valence-band barrier (Fig. 7a, b), resulting in photogenerated holes having unimpeded flow to the n^+ contact, which has the potential for high QE. However, the dark current can increase substantially at $V_d = -3.0$ V from tunneling currents which result in a lowering of QE.

OPTICAL DATA AND ANALYSIS

$InAs_{1-x}Sb_x$ with a bandgap corresponding to a cutoff wavelength of 5.05 μm at 200 K was grown on a GaAs substrate. The measured devices had the carrier wafer removed, providing the opportunity to measure detectors with the incident radiation impinging directly on the pyramid array. Knowledge of the blackbody temperature, transmission of a narrow-band filter, window transmission, Dewar geometry, and distances of the blackbody from the detector were utilized to calculate the flux incident on the detector. The photocurrent density J_{photo} as a function of bias V_d was measured at blackbody temperature settings of 400 K and 450 K, the difference between the two providing the data for the calculation of the QE versus wavelength plot shown in Fig. 8. There is no multilayer antireflective (AR) coating since the pyramids perform this function. The QE attains its maximum value of 0.82 at -1.5 V bias. As the bias increases beyond -1.5 V, the QE starts to fall since the detector tends to be increasingly dominated by tunneling currents. It is presently unclear as to what energy barriers are present to result in the requirement for a -1.5 V bias to attain peak QE. Shown in Fig. 9 is a QE versus wavelength "Data" curve for the same detector as shown in Fig. 8. Measurements were taken using a Fourier-transform infrared (FTIR) spectrometer, and the QE is seen to be high across the entire 2.0 μm to 4.6 μm band. Measurements still need to be made in the visible wavelength region.

The bandgap from Eq. 1 and the absorption coefficient from Eqs. 3 and 4 were used to calculate the QE versus wavelength curve listed as "Model" in

Fig. 9. An x value of 0.19 which results in a bandgap E_g = 247.1 meV was chosen for the "Model" curve. Since the detector has pyramids that minimize the reflectance and maximize absorption in the $InAs_{1-x}Sb_x$ material, the reflectance in the model was set at 0.05 and the effective thickness of the absorber layer was set at 7 μm. The experimental QE falls toward zero much faster than the "Model" in the 5.4 μm to 5.8 μm range. One reason could be that the absorption coefficient in that range is higher than that obtained from Eq. 3. Another potential explanation is that the absorption of the pyramid photon-trap structures is higher than that modeled by a 7-μm-thick effective absorber. There are too many fitting parameters in the absorption coefficient equation to conclude that the absorption coefficient from Eqs. 3 and 4 is the absorption coefficient of $InAs_{1-x}Sb_x$. However, it serves as a starting point for determining the absorption coefficient, which can be adjusted based on additional measurements made by varying the temperature and x value of $InAs_{1-x}Sb_x$ material.

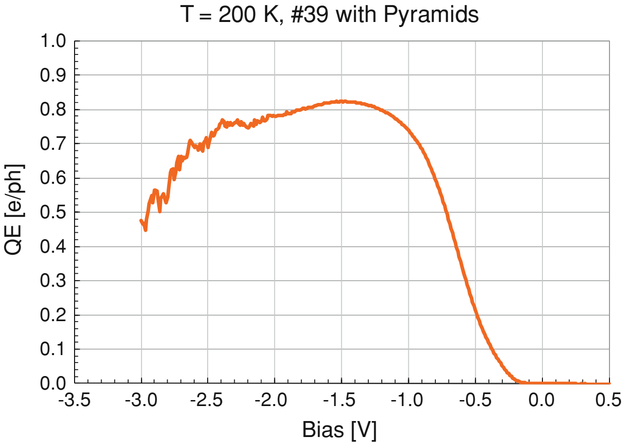

Fig. 8. QE versus V_d data calculated from J_{photo}–V_d curves.

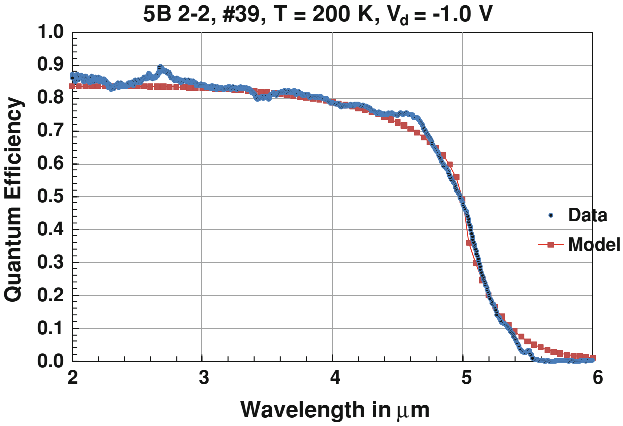

Fig. 9. QE versus wavelength model and data at 200 K and $V_d = -1.0$ V.

ELECTRICAL MODELING, DATA, AND ANALYSIS

Modeling

Device transport was modeled employing a standard formalism (see, for example, Ref. 13). The principal equations are reproduced here to clarify which physical generation–recombination mechanisms are considered, how they are treated, and to introduce parameters that appear in Table I. Poisson's Eq. 5 and the two current continuity Eqs. 6 and 7 were solved self-consistently and with Fermi statistics under steady-state conditions to simulate device transport.

$$\nabla \cdot D(x) - \rho(x) = 0, \tag{5}$$

$$\nabla \cdot (J_n(x)/q) - U_{\text{tot}}(x) = 0, \tag{6}$$

$$\nabla \cdot (J_p(x)/q) + U_{\text{tot}}(x) = 0, \tag{7}$$

where D is the electrostatic displacement, and J_n and J_p are the electron and hole current densities, respectively.

The total generation–recombination rate is

$$U_{\text{tot}} = U_{\text{SRH}} + U_{\text{rad}} + U_{\text{Auger}} - G_{\text{BBT}}, \tag{8}$$

where the Shockley–Read–Hall rate is given by

$$U_{\text{SRH}} = (np - n_i^2)/((p + n_i)\tau_{n0} + (n + n_i)\tau_{p0}), \tag{9}$$

the radiative rate is given by

Table I. Detector component-layer material parameter and fitting parameters for J_{dark}–V_d curve at 200 K

Material	m_c/m_0 [a]	m_{hh}/m_0 [a]	B (cm^3/s) (Ref. 12)	C_n (cm^6/s) (Ref. 12)	C_p	τ_{n0}	τ_{p0} (s)	A_t (V^2 s cm)$^{-1}$	B_t	C_t (V/cm)
$InAs_{0.81}Sb_{0.19}$	0.015	0.37	9.9×10^{-11}	9×10^{-27}	0	5×10^{-5}	5×10^{-7}	1.2×10^{15}	1.9	1.0×10^{6}
Compound barrier	0.13	0.43	0	0	0	5×10^{-5}	5×10^{-7}	0	0	0

[a] Computed from 14-band $k.p$ electronic structure.

$$U_{\mathrm{rad}} = B(np - n_{\mathrm{i}}^2), \tag{10}$$

the Auger rate by

$$U_{\mathrm{Auger}} = (np - n_{\mathrm{i}}^2)(nC_n + pC_p), \tag{11}$$

and the band-to-band tunneling rate is

$$G_{\mathrm{BBT}} = A_{\mathrm{t}}E^{B_t}\exp(-C_{\mathrm{t}}/E), \tag{12}$$

where n and p are the electron and hole concentrations, n_{i} is the intrinsic carrier concentration, τ_{n0} and τ_{p0} are the electron and hole SRH lifetimes, B is the radiative coefficient, C_n and C_p are the electron and hole Auger coefficients, and E is the electric field.

Data and Analysis

The dark-current density J_{dark} was measured as a function of bias V_{d} for a number detectors as a function of temperature between 140 K and 220 K. To minimize operator intervention, a semiconductor parameter analyzer in conjunction with a switching matrix was used to acquire current as a function of bias for multiple detectors in sequence at each temperature. Figure 10 plots J_{dark} versus V_{d} for one of the detectors, #39. A switching matrix is used to acquire data for a multitude of detectors sequentially, reducing time and tedium for the involved experimenter. However, the switching matrix introduces noise that is evident in the J_{dark}–V_{d} curve at 140 K. The dark-current density J_{dark} at $V_{\mathrm{d}} = -1.5$ V is plotted versus 1000/T in Fig. 11 to extract the activation energy at the bias at which QE attained its maximum value. From Fig. 11, the activation energy $E_{\mathrm{a}} = 275.9$ meV is extracted, which is close to the bandgap E_{g} ($x = 0.19$, $T = 0$ K) = 269.8 meV, suggesting that the dominant dark current at $V_{\mathrm{d}} = -1.5$ V is a diffusion current.

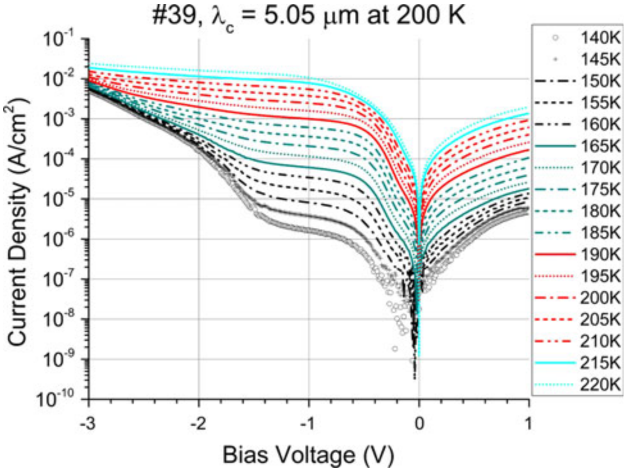

Fig. 10. Dark-current density J_{dark}–V_{d} curves as a function of temperature for an nCBn (5.05 μm at 200 K) InAs$_{1-x}$Sb$_x$ photon-trap structure detector.

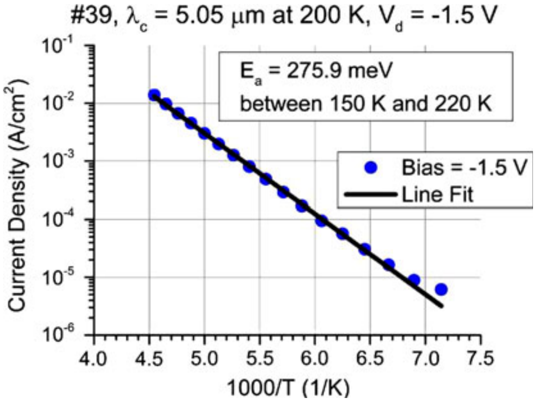

Fig. 11. Dark-current density J_{dark}–T at $V_{\mathrm{d}} = -1.5$ V provides activation energy $E_{\mathrm{a}} = 275.9$ meV.

Figure 12a compares device transport simulations with experimental J_{dark} versus temperature at $V_{\mathrm{d}} = -1.5$ V. There is good agreement at the higher temperatures, with some deviation as the temperature is decreased, the experimental values of J_{dark} being lower than the simulated values. Figure 12b is a plot of the simulated and experimental J_{dark}–V_{d} at $T = 200$ K. The fit is good at large bias values, however the experimental values deviate from the simulation at reverse-bias values less than ~0.5 V. Lower experimental J_{dark} as compared with simulation in the ~0.2 V to 0.5 V reverse-bias range is probably caused by the same barrier that limits the QE from not attaining a maximum value until the bias is −1.5 V. Table I specifies the input parameters employed to compute the dark-current density J_{dark}–V_{d} curve at 200 K. The properties (including the conduction electron and heavy hole effective masses m_{c} and m_{hh}, respectively, relative to the free electron mass m_0) were obtained from the cited sources. The last four columns are fitted parameters to reproduce the J_{dark}–V_{d} for detector #39. Zero values specify quantities that are not expected to affect results. Figures 13a, b, and 14a, b are plots of dark-current density J_{dark} versus 1000/T that are used to extract the activation energy at −0.2 V, −0.4 V, −1.4 V, and −3.0 V, respectively. The activation energy $E_{\mathrm{a}}(V_{\mathrm{d}} = -0.2\ \mathrm{V}) = 331.9$ meV is close to the bandgap energy and valence-band barrier of 356 meV (Fig. 6a). However, at $V_{\mathrm{d}} = -0.4$ V, there is virtually no valence-band barrier (Fig. 6b), so the reason for the activation energy $E_{\mathrm{a}}(V_{\mathrm{d}} = -0.4\ \mathrm{V}) = 342.7$ meV is not well understood (Fig. 13b). As expected from the dominance of diffusion current at $V_{\mathrm{d}} = -1.4$ V, $E_{\mathrm{a}}(V_{\mathrm{d}} = -1.4\ \mathrm{V}) = 278.9$ meV is close to the bandgap energy, $E_{\mathrm{g}}(x = 0.19,\ T = 0\ \mathrm{K}) = 269.8$ meV. At $V_{\mathrm{d}} = -3.0$ V, the dark-current density has minimal temperature dependence, a characteristic of tunneling currents, a consequence of the conduction- and valence-band lineup seen in Fig. 7b.

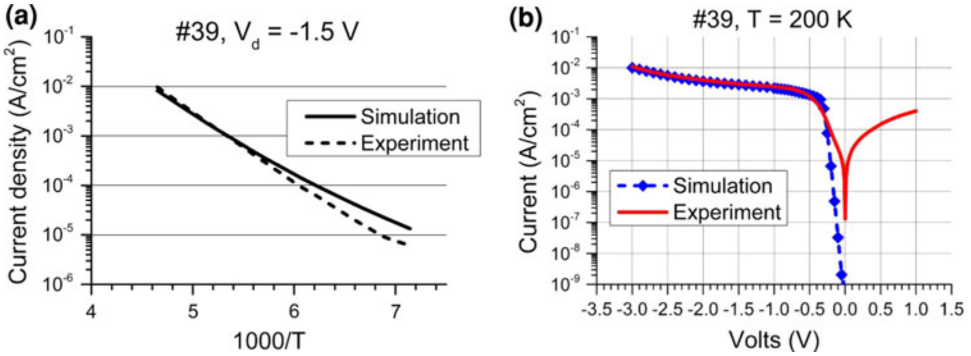

Fig. 12. Simulated and measured (a) dark current density J_{dark} versus temperature at $V_d = -1.5$ V and (b) J_{dark}–V_d curve at $T = 200$ K for $N_d = 1.0 \times 10^{15}$ cm^{-3}.

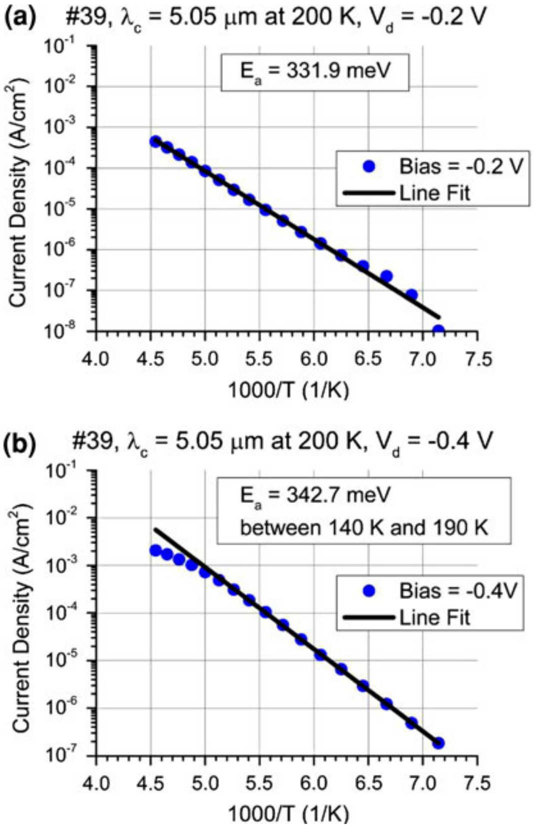

Fig. 13. Dark-current density J_{dark}–T at (a) $V_d = -0.2$ V and (b) $V_d = -0.4$ V to determine activation energy.

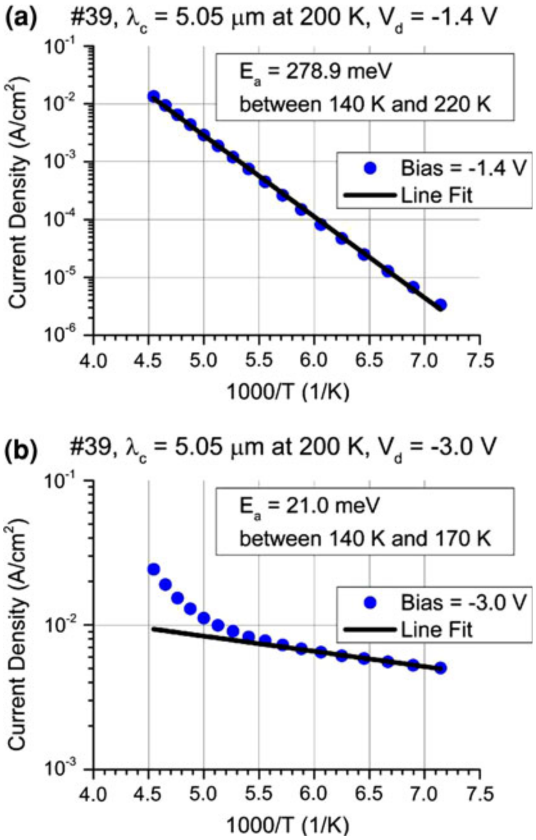

Fig. 14. Dark-current density J_{dark}–T at (a) $V_d = -1.4$ V and (b) $V_d = -3.0$ V to determine activation energy.

CONCLUSIONS

$\mathrm{InAs}_{1-x}\mathrm{Sb}_x$ nCBn detectors with cutoff wavelengths in the 5-μm range at 200 K were fabricated and characterized for optical properties and electrical performance as a function of temperature. Absorption coefficient information from the literature and spectral response measurements of the MWIR nCBn detectors were combined to propose an absorption coefficient $\alpha(E, x, T)$ model. Additional measurements of material and detectors with different x values and as a function of temperature are needed to provide a more accurate value of the absorption coefficient. Band structures were computed using a $k{\cdot}p$ formalism, and from the band structure, the dark-current density as a function of bias and temperature was simulated and compared with J_{dark}–V_{d} curves at fixed T and J_{dark}–T curves at constant V_{d}. There is a good match between simulation and data over a wide range of bias, but between -0.4 V and zero bias, simulations and experiment diverge. Activation energy for the dark current was extracted at various biases using the

J_{dark}–V_{d} measurements with temperature as a parameter. The dark-current activation energy E_{a} at $V_{\mathrm{d}} = -0.2$ V seems to be a function of the bandgap plus a valence-band barrier. At $V_{\mathrm{d}} = -0.4$ V, the high E_{a} is not yet understood. E_{a} is approximately equal to the bandgap in the −1.4 V to −1.5 V range, where the dominant dark current is a diffusion current and the QE is high. Tunneling dominates the dark current at $V_{\mathrm{d}} = -3.0$ V as expected from the band profile and confirmed by the low activation energy value.

ACKNOWLEDGEMENTS

This work was supported by DARPA under Contract N66604-09-C-3652 (Dr. Nibir Dhar, DARPA Program Manager). However, the views expressed are those of the author and do not reflect the official policy or position of the Department of Defense or the US Government. This is in accordance with DoDI 5230.29, January 8, 2009. Special thanks go to Mr. Dan Okerlund, the ever-patient Program Manager at DRS, Dr. Ravi Dat, Booz Allen Hamilton for technical and other advice, and Ms. Yesim Anter for helping prepare the manuscript. Excellent work was performed by Prof. Saif Islam and his team at UC Davis, who were instrumental in different aspects of the processing sequence.

REFERENCES

1. S. Maimon and G.W. Wicks, *Appl. Phys. Lett.* 89, 151109 (2006).
2. A.M. White, USA Patent No. 4,679,063 (1987).
3. A.I. D'Souza, A.C. Ionescu, M. Salcido, E. Robinson, L.C. Dawson, D.L. Okerlund, T.J. de Lyon, R.D. Rajavel, H. Sharifi, D. Yap, M.L. Beliciu, S. Mehta, W. Dai, G. Chen, N. Dhar, and P. Wijewarnasuriya, *Proc. SPIE* 8012, 80122S (2011).
4. H.H. Wieder and A.R. Clawson, *Thin Solid Films* 15, 217 (1973).
5. A. Rogalski, *Prog. Quant. Electr.* 13, 191 (1989).
6. J.R. Dixon and J.M. Ellis, *Phys. Rev.* 123, 1560 (1971).
7. G.B. Stringfellow and P.E. Greene, *J. Electrochem. Soc.* 118, 805 (1971).
8. K. Moazzami, J. Phillips, D. Lee, S. Krishnamurthy, G. Benoit, Y. Fink, and T. Tiwald, *J. Electron. Mater.* 34, 773 (2005).
9. F. Urbach, *Phys. Rev.* 92, 1324 (1953).
10. J.T. Olesberg (Ph.D. Thesis, University of Iowa, 1999).
11. C.W. Cheah, L.S. Tan, and G. Karunasiri, *J. Appl. Phys.* 91, 5105 (2002).
12. http://www.ioffe.ru/SVA/NSM/Semicond/ with Vegard's law applied. Accessed July 5, 2012.
13. C.M. Snowden, *Semiconductor Device Modeling*. Technology & Engineering (Springer-Verlag, 1989).